American Mineralogist, Volume 84, pages 970–976, 1999

Raman spectra and vibrational analysis of the trioctahedral mica phlogopite

DAVID A. MCKEOWN,[1,*] MICHAEL I. BELL,[2] AND EDGAR S. ETZ[3]

[1]Vitreous State Laboratory, Catholic University of America, 620 Michigan Avenue N.E., Washington, D.C. 20064, U.S.A.
[2]Naval Research Laboratory, Dynamics of Solids Branch, Code 6680, Washington, D.C. 20375-5320, U.S.A.
[3]Surface and Microanalysis Science Division, National Institute of Standards and Technology, Gaithersburg, Maryland 20899-0001, U.S.A.

ABSTRACT

Raman spectra were measured and normal mode calculations were performed for phlogopite. Calculated fundamental mode frequencies were fit to observed frequencies assigned to features in the two polarized Raman spectra collected, so that unambiguous assignment of eigenmodes could be made to nearly all Raman spectral features. Average force constant values determined for Si-O and O-Si-O environments as well as for the non-silicate environments in cyclosilicates and gillespite provided an excellent starting point for the phlogopite calculations that quickly converged to a best fit of theoretical mode frequencies to the observed Raman fundamental mode frequencies. Final values of the force constants for T-O stretch and O-T-O bend are within the range of force constant values determined for Si-O and O-Si-O environments in cyclosilicates and gillespite. The force constant similarities extend to the K-O, M(1,2)-O bond stretch and M(1,2)-O-T bond bend environments. Raman-active modes at frequencies greater than 850 cm^{-1} are localized intra-sheet modes dominated by T-O stretch and O-T-O bend motions. Raman-active modes between 350 and 850 cm^{-1} are dominated by mixtures of internal sheet modes with displacements from the M2 sites. Raman-active lattice modes are calculated at frequencies less than 350 cm^{-1}. Calculated frequencies for the IR-active A_u and B_u, modes generally fall within the frequency ranges of broad bands in the IR spectra for phlogopite presented elsewhere. Eigenmodes calculated for phlogopite are generally unique to that mica structure and differ from those determined for the cyclosilicates and gillespite. The few eigenmodes calculated for phlogopite that resemble those calculated for the cyclosilicates are the most localized T-O stretch motions and are assigned to the highest frequency modes.

INTRODUCTION

This work describes measurements of the Raman spectra and calculations of the zone-center optical phonons of the trioctahedral mica phlogopite. The motivation of this work is to provide vibrational assignments to the Raman spectra of phyllosilicate minerals, which contain sheets of linked silicate and aluminate tetrahedra. Mica structures represent the next higher level of complexity with respect to silicate tetrahedral polymerization when compared to cyclosilicate structures studied in our previous work (Kim et al. 1993, 1995; McKeown et al. 1995, 1996; McKeown and Bell 1997). In moving to this next level of complexity, one objective is to determine whether mica structures exhibit force constant values and atomic displacements (eigenmodes) similar to those found in cyclosilicates. The Raman and IR spectra of phlogopite were presented earlier by Loh (1973) and Clemens et al. (1987) and their results are compared with the data collected and calculations obtained in this study.

The crystal structure of phlogopite has monoclinic C2/*m* symmetry and is comprised of tetrahedral sheets that are bonded together by alternating layers of K^+ and Mg^{++} ions as shown in Figure 1 (Hazen and Burnham 1973). The sample used in the present study is the same one used in the structure determination work by Hazen and Burnham and has the chemical formula: $(K_{0.76}Na_{0.16}Ba_{0.05}\square_{0.03})Mg_3(Si_3Al)O_{10}[F_{1.3}(OH)_{0.7}]$. The sheets contain tetrahedral sites (T), where 75% are randomly occupied by Si and the remaining 25% contain Al. Each tetrahedron has one non-bridging O atom, Onb (O3), and three bridging O atoms, Ob (two O1 and one O2), which are shared with three other tetrahedra. The tetrahedra link to form six-membered rings that are each connected to six other symmetrically equivalent six-membered rings. The K sites are coordinated to six O atoms within the tetrahedral sheets: four O1 and two O2. The Mg cations are located in the two octahedral sites, M1 and M2, that form a trioctahedral layer between the tetrahedral sheets; each Mg is coordinated by four O3 atoms from the tetrahedral sheets and two (F,OH) sites.

FACTOR GROUP ANALYSIS

Factor group analysis (FGA) was performed for the phlogopite structure using the method of Fateley et al. (1972). The results are given in Table 1, where the contributions from K, Ml, M2, T_4O_{10} sheets, and (F,OH) are listed separately. The normal modes are divided into 60 nondegenerate modes ($14A_g + l3B_g + 14A_u + 19B_u$), including three acoustic modes, one A_u and two B_u. As indicated in Table 1, the A_g and B_g modes are Raman active, and the A_u and B_u modes are IR-active. Due to site symmetry, the Raman-active A_g and B_g modes have no contributions from K or M1, while the IR-active A_u and B_u modes have contributions from all atomic sites in the structure.

*E-mail: davidm@rsrch.vsl.cua.edu

EXPERIMENTAL METHODS

The phlogopite crystal used in this study is a pale pink plate that was collected at Franklin, New Jersey (Harvard Museum sample no. 99276, supplied by the Mineral Sciences Department, National Museum of Natural History, Smithsonian Institution). The plate is approximately 6 mm × 6 mm × 4 mm. The sample was characterized by Hazen and Burnham (1973).

Polarized single crystal Raman spectra were obtained from the oriented single crystal in back scattering geometry using a Bruker FT-Raman instrument (Model RFS-100). The source was a Nd:YAG laser supplying 1064 nm wavelength excitation at 600 mW. Variable power densities were initially placed at the sample to make sure that no sample modification was incurred. The detection system consisted of a high sensitivity germanium detector operated at liquid nitrogen temperatures. All spectra were recorded at 4 cm^{-1} resolution and were corrected for the instrument response function. Raman shift calibration ensured that band frequency positions are accurate to within 1 cm^{-1}. In each scattering geometry, the FT-Raman spectrum was acquired through 640 coadded scans to optimize signal-to-noise. Using near-IR excitation furnished spectra essentially free of laser-induced luminescence from the sample. Earlier measurements on the same mineral specimen using 514.5 nm laser excitation produced inferior spectra characterized by a broad band luminescent background that masked many of the Raman spectral features.

The flat surface of the crystal was oriented perpendicular with respect to the incident and scattered light propagation directions. The Raman spectra are shown in Figure 2, where the notation in the upper right portion of the plots (Figs. 2b and 2c) denotes the incident and scattered light propagation and polarization directions. This notation is consistent with the axis labeling convention in Figure 1 where the *y* or *b* axis is parallel to the twofold rotation axis of the crystal. The procedure for determining the vibrational species contributing to each polarized Raman spectrum is outlined in Loudon (1964).

The Raman spectra collected are similar to those presented by Clemens et al. (1987) and Loh (1973) but provide good signal-to-noise over a larger frequency range, especially near the laser line. Significant intensity differences of Raman spectral features exist among the three studies, especially between this study and Loh's work, for the most prominent peaks near 100, 192, 358, and 682 cm^{-1}. These spectral variations may be due to various reasons: different spectrometers and laser excitation lines used to collect the data, different sample scattering conditions and resulting Raman tensor components that affect the spectra, or chemical and structural differences among the samples studied.

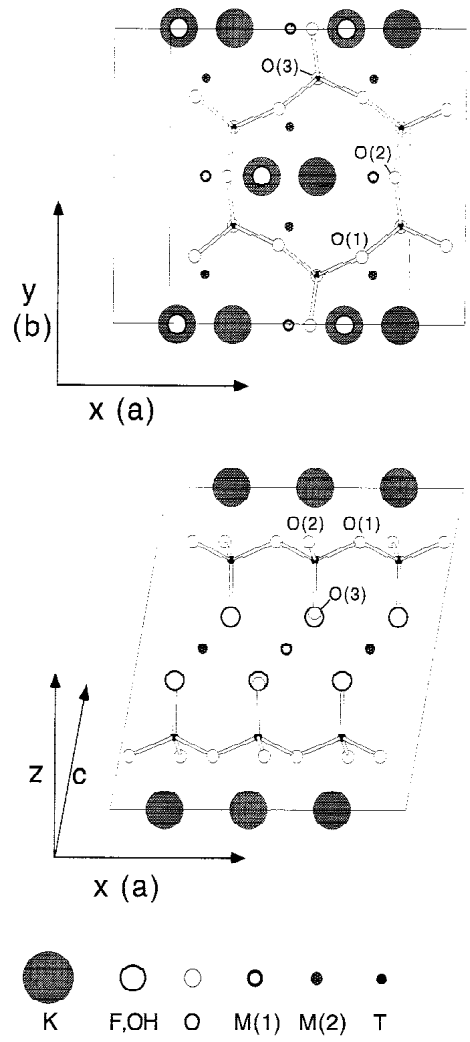

FIGURE 1. The phlogopite structure. The *x* and *y* axes used in the calculations are parallel to the *a* and *b* axes, respectively, of the crystal structure. The calculations used cartesian coordinates and an orthogonal coordinate system, hence the *z* axis is not coincident to the *c* axis of the monoclinic crystal structure. The top view is the *z* axis projection, where only the top tetrahedral sheet is shown for clarity. The bottom view is the *y* axis projection. All T-O bonds and the oxygen labeling conventions are indicated.

TABLE 1. The irreducible representations of phlogopite

	A_g(R)	B_g(R)	A_u(IR)	B_u(IR)
K	0	0	1	2
M1	0	0	1	2
M2	1	2	1	2
F,OH	2	1	1	2
T_4O_{10} sheet	11	10	10	11
Total	14	13	14*	19†

Notes: Species followed by the notation (R) or (IR) are Raman or infrared active, respectively.
* One of the A_u modes is acoustic.
† Two of the B_u modes are acoustic.

Loh's z(yy)x spectrum for clear phlogopite is equivalent to the polarization conditions for the A_g spectrum in Figure 2b. However, Loh's spectrum has no evidence of the strong 199 cm^{-1} A_g line. Our A_g spectrum more closely resembles Loh's y(zz)x data. A very weak feature near 162 cm^{-1} in the A_g spectrum appears to correspond to the strong 162 cm^{-1} peak in Loh's z(yy)x spectrum. This strong 162 cm^{-1} peak is not evident in any of the spectra gathered for this study, and was not observed at all by Clemens et al. Comparing parallel polarized with crossed polarized spectra for clear phlogopite in Loh's Figure 3, the 107 cm^{-1} peak in-

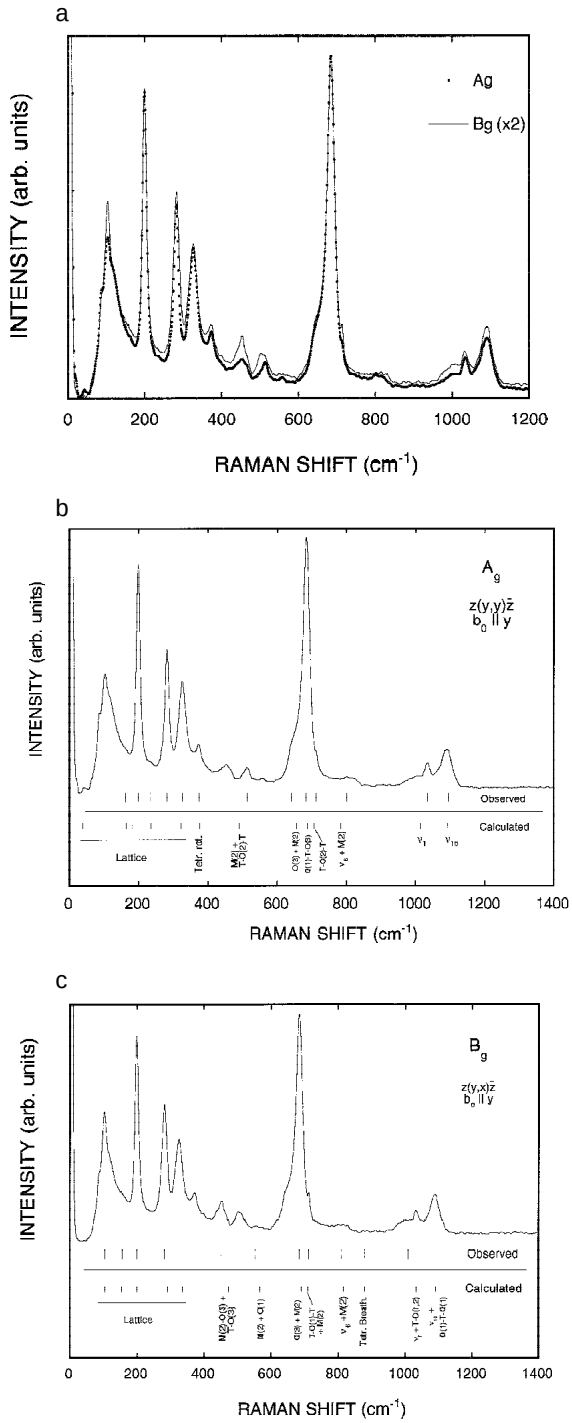

FIGURE 2. The Raman spectra of phlogopite. **(a)** Comparison plot of A_g and B_g symmetry spectra; **(b)** A_g and **(c)** B_g symmetry observed and calculated Raman-active modes. Long vertical bars labeled as "observed" are the Raman fundamental mode frequencies. Short vertical bars labeled as "calculated" are the theoretical frequencies with some vibrational assignments from the normal coordinate analysis. The spectra were collected with **(b)** incident and scattered light polarized parallel to [010] and **(c)** incident light polarized parallel to [010] and scattered light polarized parallel to [100].

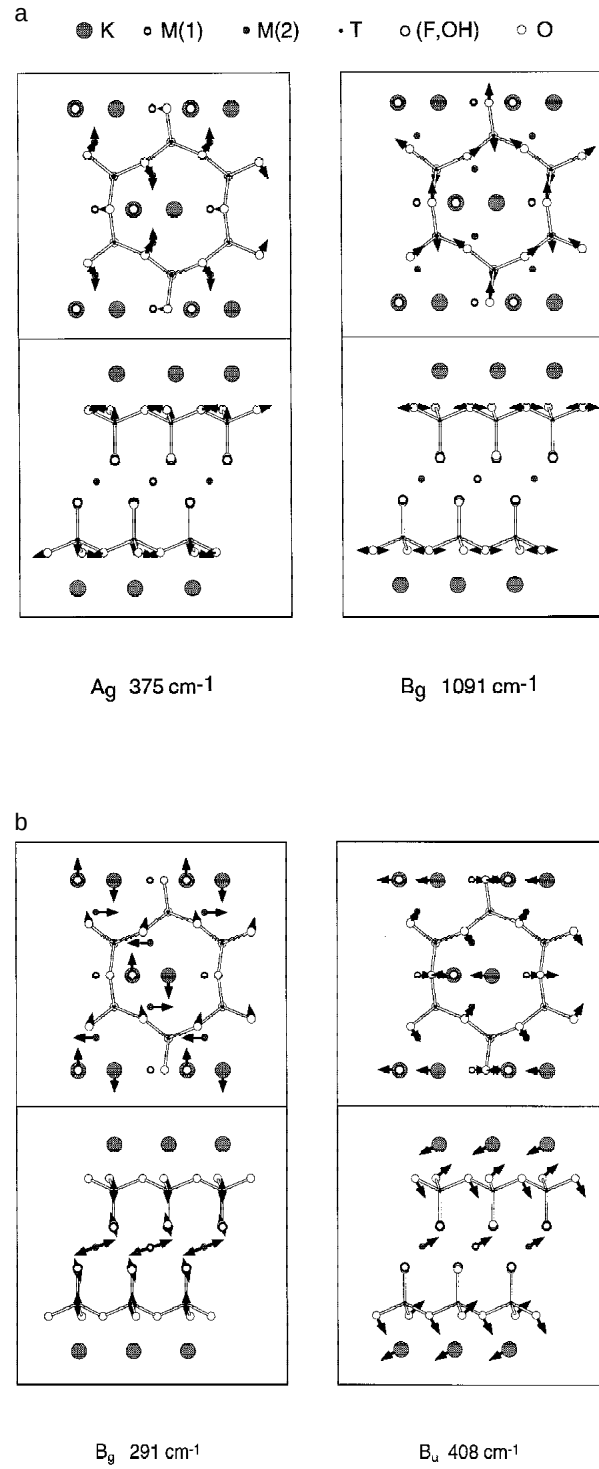

FIGURE 3. (**a**) Calculated atomic motions for the normal modes internal to the silicate sheets in the phlogopite structure. The diagrams in the upper and lower boxes are the *z* axis and the *y* axis projections, respectively. In the *z* axis projection, only the top tetrahedral sheet of the two in the cell is drawn for clarity. Arrows are drawn to scale, indicating the relative amplitude of the motion for each atom. (**b**) Examples of lattice vibrational modes; conventions in Figure 3a apply.

creases its relative intensity with respect to other strong features in the crossed polarized spectrum. This polarization dependence is seen in Figure 2a, but to a much weaker degree compared with that shown by Loh. Our 105 cm^{-1} peak increases its intensity in the crossed polarized B_g spectrum with respect to other features in the parallel polarized A_g spectrum.

Clemens et al. (1987) and Loh (1975) provide only partial listings of observed Raman mode frequencies, but from this we can make some comparisons. Raman active mode frequencies at 162, 196, 685, and 1035 cm^{-1} listed by Loh for clear phlogopite and at 192 and 682 cm^{-1} listed by Clemens et al. correspond with our observed A_g modes near 162, 199, 684, and 1034 cm^{-1}. Raman active mode frequencies at 107, 157, 200, and 279 cm^{-1} listed by Loh for clear phlogopite and at 100 and 192 cm^{-1} listed by Clemens et al. correspond to our observed B_g modes near 105, 155, 199, and 282 cm^{-1}.

NORMAL COORDINATE ANALYSIS

A cluster of the 39 atoms simulating the phlogopite structure was used for the lattice dynamics calculations at zero wavevector, following the procedure reported elsewhere (Kim et al. 1993). This cluster consisted of 19 more atoms than the primitive cell [12 more O atoms, four more tetrahedral sites, and three more (F,OH) sites] to complete the K, Ml, and M2 coordination environments; this was done so that the programs performed the calculations properly. Any two atoms in the cluster that are related to each other by a unit-cell translation were input as equivalent atoms; these atoms have the same motion in the resulting eigenmodes.

The potential energy model used to describe the bonding is based on a valence force potential consisting of bond-stretching and bond-bending interactions. A total of 76 interactions were defined for the calculation that adequately describe the bonding environments in the phlogopite structure in the sense that all fundamental optical modes are calculated to have nonzero frequencies. The crystal structure of phlogopite contains sites that are occupied by more than one atom type. Accordingly, the calculations were set-up by using weighted averages of the masses for the atom types that occupy the K, T, and (F, OH) sites, from the chemical formula above.

The total number of Raman-active fundamental modes predicted by FGA for the phlogopite structure (27) is larger than the number of spectral features (18) clearly observed in the Raman spectra (Fig. 2) that can be considered as fundamental modes. The calculations indicate, however, that eight peaks can be assigned to both A_g and B_g modes. The selection of fundamental frequencies in the Raman spectra to be used as targets for the calculation was relatively simple, because all modes observed in the data were close to initial theoretical fundamental frequencies calculated by the program. There is no evidence of combination or overtone modes in the data. Variations between the A_g and B_g spectra are subtle (see Fig. 2a), where the most noticeable differences are intensity differences as well as small frequency shifts and shape changes for some peaks. In most cases, the frequencies determined from the spectral features provided guidelines and constraints for the calculated frequencies. The calculations provided guidelines for selecting species assignments to the weak spectral features at 162 and 234 cm^{-1} (A_g modes) and at 155, 554, and 880 cm^{-1} (B_g modes).

We performed initial lattice dynamics calculations for the phlogopite structure using force constant values for T-O, K-O, and M-O stretching and O-T-O and M-O-T bending similar to those determined for equivalent environments in the crystal structures investigated previously. These initial values provided a good starting point for the calculations, as the program converged rapidly to a best fit of the theoretical Raman-active mode frequencies to the observed frequencies.

Ten force constants were adjusted to give the best fit between calculated and observed frequencies in the two Raman spectra. The fitting was accomplished by minimizing the root-mean-square (rms) deviation between the calculation and measurement (Kim et al. 1993). Before the best fit was obtained, a model containing eleven force constants was run, where the two M-O-T force constants M1-O-T and M2-O-T were refined separately. This resulted in the Ml-O-T force constant being driven to zero. Examining the Ml-O-T and M2-O-T bonding in the crystal structure, it is difficult to explain why one set of these environments should be very different from the other. It was also not possible to eliminate the M-O-T force constants altogether from the calculation, despite their small values, because optical modes with zero frequency would be generated. To eliminate this problem, all M-O-T force constants were linked together. Non-zero values were then obtained for all 10 final force constants (Table 2), and the rms deviation converged to 11.6 cm^{-1}. The calculated frequency and the associated eigenmode for each Raman-active fundamental mode is listed in Tables 3 and 4, and plotted in Figures 2b and 2c. Calculated frequencies and mode assignments for the IR-active A_u and B_u species are also presented for completeness in Tables 5 and 6, respectively, and are compared with the IR data presented by Loh (1973), Clemens et al. (1987), and Tateyama et al. (1977). The fitting routine was run with force constants for the M1 and M2 environments that were linked together so that only eight force constants were varied. The results of this fitting led to an rms deviation of 13.6 cm^{-1} and force constant values within several per cent of those listed in Table 2. Due to the worse rms deviation for the linked M-site case, we only present here the results for the 10 force constant model. The normal mode frequencies and eigenvectors were also calculated for the isolated tetrahedral sheets by gradually reducing all force constants involving K, M1, and M2 to zero.

TABLE 2. Force constant values determined for phlogopite resulting in a rms deviation of 11.6 cm^{-1}

Force constant	Interaction	Value
k_1	T-O3	4.55×10^5 dyne/cm
k_2	T-O1,2	4.05×10^5 dyne/cm
k_3	M1-O3	2.50×10^5 dyne/cm
k_4	M2-O3	2.11×10^5 dyne/cm
k_5	M1-F,OH	0.58×10^5 dyne/cm
k_6	M2-F,OH	0.36×10^5 dyne/cm
k_7	K-O1,2	1.51×10^5 dyne/cm
k_8	O1,2-T-O3	2.08×10^{11} erg
k_9	O1,2-T-O1,2	0.21×10^{11} erg
k_{10}	M-O3-T	0.11×10^{11} erg

TABLE 3. Observed and calculated Raman-active A_g mode frequencies and assignments for phlogopite

z(y,y) $\bar{z}$ Experimental (cm^{-1})	Calculated (cm^{-1})	Assignment
–	38	M2*y*-trans. + (F,OH)*c*-trans. + sheet *c*-trans.
162	164	(F,OH)*c*-trans. + sheet *z*-trans. + tetrahedral rot. ÷ ÷*z*
199	182	sheet *xz*-trans. + (F,OH)*z*-trans.
234	235	(F,OH)*xz*-trans.
282	271	M2*y*-trans. + (F,OH)*x*-trans. + sheet *y*-def.
326	322	O2*x*-trans. + M2*y*-trans.
373	375	tetrahedral rot. ÷ ÷*z* + M2 *y*-trans.
513	490	M2*y*-trans. + T-O2-T bend
641	656	O3*x*-trans. + M2*y*-trans.
684	687	O3-T-O1 bend
712	707	T-O2-T bend
801	784	v_6 along *y* + M2*y*-trans.
1034	1013	T-O3 stretch (v_1)
1094	1092	T-O1 stretch (v_{10})

Notes: The more dominant displacements are listed first. trans. = translatory motion; rot. = hindered rotation; def. = deformation.

TABLE 4. Observed and calculated Raman-active B_g mode frequencies and assignments for phlogopite

z(y,y) $\bar{z}$ Experimental (cm^{-1})	Calculated (cm^{-1})	Assignment
105	105	(F,OH)*y*-trans. + M2*c*-trans. + O3*xy*-trans.
155	154	M2*xz*-trans. + O3-*xz*-trans. + O1*x*-trans. + (F,OH)*y*-trans.
199	199	(F,OH)*y*-trans. + T-O3*y*-trans.
282	291	M2*x*-trans. + (F,OH)*y*-trans. + O1-T-O1 bend
326	335	O1-T-O1 bend + M2*z*-trans.
452	473	M2-O3 stretch + T-O3*xz*-4trans.
554	567	M2*xz*-trans. + O1*c*-trans.
641	690	O3*y*-trans. + M2*xz*-trans.
712	710	T-O1-T bend + M2 *xz*-trans.
810	816	v_6 along *x* +| M2 *xy*-trans.
880	880	tetrahedral breathing + (minor: M2*x*-trans.)
1008	1033	T-O3 stretch (v_1) + T-O1,2 stretch
1090	1091	T-O2 stretch (v_{10}) + O1-T-O1 bend

Note: Conventions in Table 3 apply.

TABLE 5. Observed and calculated IR-A_u mode frequencies and assignments for phlogopite

Experimental (cm^{-1})	Calculated (cm^{-1})	Assignment
–	138	K *y*-trans. + M2-*y*-trans. + (F,OH)-y-trans. + O1-T-O1 bend
161†	165	M1*y*-trans. + (F,OH)-*y*-trans. + K-*y*-trans. + M2-*y*-trans.
250†	246	(F,OH)*y*-trans. + M1*y*-trans. + M2-*y*-trans. + O3*x*-trans.
275† ?	321	M1*y*-trans. + M2*y*-trans. + v_6 along *y*
broad band *†	361	M2-*y*-trans. + O1-T-O1 bend + T-O3*z*-trans. + K *y*-trans.
broad band *†	474	K *y*-trans. + M1*y*-trans. + O1-T-O1 bend + M2-*y*-trans.
broad band *†	570	M1-*y*-trans. + M2 *y*-trans. K *y*-trans. + O1-T-O1 bend
700 *†	713	T-O1-T bend + K *y*-trans.
–	772	M1*y*-trans. + M2*y*-trans. + v_6 along *x*
800 *†	809	M1-O3 stretch + v_6 along *x*
–	884	tetrahedral breathing + M1 *y*-trans.
broad band *†	1035	T-O3 stretch (v_1) + T-O1,2 stretch
broad band *†	1092	T-O2 stretch(v_{10}) + O1-T-O1 bend

Note: Conventions in Table 3 apply.
* Experimental frequencies are from Clemens et al. (1987).
† Experimental frequencies are from Loh (1973).

DISCUSSION

Force constant values

An objective of this study is to determine whether the force constant values calculated earlier for several cyclosilicates and gillespite are transferable to mica structures. The final force constant values determined here (Table 2) indicate that this is the case for phlogopite on several levels. The magnitudes of the bond stretch force constants for phlogopite are within the range of equivalent force constant values calculated for the other structures. The agreement is not as good for the bond bending force constants, but those calculated for phlogopite are not significantly larger or smaller than those presented for the cyclosilicates and gillespite. Force constant similarities are observed down to the smallest values determined for phlogopite: where the M-O-T value is similar to metal-O-Si values calculated earlier.

Frequencies of calculated modes vs. observed Raman- and IR-active modes

The calculations fit theoretical fundamental mode frequencies to the observed mode frequencies in the two polarized Raman spectra so that eigenmodes are unambiguously assigned to virtually all peaks in the spectra (Figs. 2b and 2c). The calculations placed an A_g mode at 38 cm^{-1} that appears to correspond to a small polarized Raman peak near 43 cm^{-1} in the A_g spectrum (Fig. 2a). We cannot confidently assign this feature to an A_g fundamental mode, however, due to the filter cut-off of the FT-Raman instrument at 85 cm^{-1}. The small peak near 558 cm^{-1} appears to be an A_g mode, based on comparison of the relative intensities of this feature with respect to background in the A_g and B_g spectra (Fig. 2a). On the other hand, the calculations place B_g mode near this feature; so we assign it as a B_g mode. The assignment

TABLE 6. Observed and calculated IR-B_u mode frequencies and assignments for phlogopite

Experimental (cm^{-1})	Calculated (cm^{-1})	Assignment
–	29	(F,OH)*xz*-trans. + M1*x*-trans.
–	75	K *z*-trans. + tetrahedral rot. ÷ ≠
90†‡	85	(F,OH)*x*-trans. + M1 *z*-trans. + M2 *xz*-trans. + O3 *y*-trans.
156†‡	156	K *x*-trans. + O1-T-O2 bend + M1 *xz*-trans. + O3 *x*-trans.
195†	183	(F,OH)c-trans. + M1 *x*-trans.
275†?	320	M1*z*-trans. + v_6 along *x* + M2 *x*-trans.
broad band*†	365	M1*xz*-trans. + (F,OH)-*xz*-trans. + M2 *xz*-trans.
broad band*†	381	M1*x*-trans. + M2 *z*-trans. + K-*z*-trans. + (F,OH)*x*-trans. + O2 *xz*-tran.
broad band*†	408	M1*xz*-trans. + K-*xz*-trans. + O1-T-O2 bend
broad band*†	514	Tetrahedral rot. ≡ *z* + M2 *z*-trans. + K *z*-trans. + M1 *xz*-trans.
broad band*†	584	M2*xz*-trans. + K *x*-trans. + O1-T-O2 bend
700†	716	T-O2-T bend
–	730	T-O3c-trans. + O1,2-c-trans.
800†	800	M2-O3 stretch along *x*
826*	837	v_6 along *y* + M1*xz*-trans.
broad band*†	1030	T-O3 stretch (v_1)
broad band*†	1093	T-O1 stretch(v_{10})

Note: Conventions in Table 3 apply.
* Experimental frequencies are from Clemens et al. (1987).
† Experimental frequencies are from Loh (1973).
‡ Experimental frequencies are from Tateyama et. al (1977).

of a B_g mode near 880 cm^{-1} in the data was influenced by the calculation placing a fundamental mode at this frequency. We might also justify this assignment on the basis of the small increase of intensity at this frequency in the B_g spectrum relative to the A_g spectrum (Fig. 2a).

Observed IR fundamental mode frequencies were not used in the fitting process, but we can compare our calculated A_u and B_u mode frequencies with the IR data presented by Loh (1973) and Clemens et al. (1987). Low frequency IR-modes observed by Loh near 89 and 92 cm^{-1} may correspond to our B_u calculated mode at 85 cm^{-1}. IR-active mode frequencies listed by Loh at 154, 161, 195, 220, and 275 cm^{-1} appear to correspond to our calculated A_u modes at 165, 246, and 321cm^{-1} and to our calculated B_u modes at 156,183, and 320 cm^{-1}. Clusters of higher frequency IR modes determined by our calculations can be assigned to broad features in the IR spectra (Fig. 6 in Loh 1973). Broad bands reported by both Loh and Clemens et al. from approximately 365 to 600, 700, 800, and from 950 to 1100 cm^{-1} appear to be reasonable matches to our calculated A_u modes at 361, 474, 570, 713, 772, 1035, and 1092 cm^{-1} and to our calculated B_u modes at 365, 381, 408, 514, 584, 716, 837, 1030, and 1093 cm^{-1}.

Eigenmode descriptions and assignments

Several trends can be seen in the eigenmodes calculated for phlogopite and assigned to features in our Raman spectra and the IR spectra presented in the literature. Considerable mixing of K, Ml, and M2 displacements with those from the tetrahedral sheets are found for modes as high as 850 cm^{-1}. At the highest frequencies, modes become localized within the tetrahedral sheets and are dominated by T-O stretch displacements. We briefly compare our eigenmode assignments to assignments discussed in Loh's study, the only reference (to our knowledge) where vibrational assignments were made to some observed Raman- and IR-active modes.

Raman-active A_g and B_g species eigenmodes can be grouped into three frequency ranges according to the dominant atomic displacements. The characteristics of these groups differ, however, from the corresponding groups found in cyclosilicates and gillespite. Modes at frequencies greater than 850 cm^{-1} are localized T-O stretch as well as O-T-O bend motions internal to the sheets (Fig. 3a, right). Modes between 350 and 850 cm^{-1} have bond stretch and bend motions within the T_4O_{10} sheets and M2 octahedra. Modes at frequencies less than 350 cm^{-1} vary to zero frequency when all force constants involving K, M1, and M2 environments are varied to zero; these are classified as lattice modes, where longer-range T_4O_{10}, sheet motions can mix with M2 and (F,OH) displacements (Fig. 3b, left).

IR-active A_u or B_u species eigenmodes can also be grouped into similar frequency ranges. Above 800 cm^{-1}, modes are dominated by T-O stretch and O-T-O bend motions internal to the sheets. Below 800 cm^{-1}, modes can contain mixtures of K, Ml, M2, and internal sheet motions. At frequencies below 450 cm^{-1}, lattice modes dominate, that can contain motions from all atoms in the crystal structure (Fig. 3b, right).

At frequencies above 1000 cm^{-1}, modes internal to the tetrahedral sheets occur as A_g-B_u and B_g-A_u pairs; the major difference between the modes within a pair is that the displacements in two neighboring sheets are in-phase with each other in one mode (A_g or B_u) and out-of-phase in the other mode (A_u or B_g). The frequencies of these mode pairs are similar (compare Tables 3 with 6 and Tables 4 with 5). Such A_g-B_u and B_g-A_u, mode pairs clearly occur down to approximately 700 cm^{-1}. Below 700 cm^{-1}, the mode pair relationships become obscured when motions from the K and octahedral environments mix with the internal sheet modes.

Specific eigenmode assignments made to Raman and IR modes in this study do not agree particularly well with assignments made by Loh (1973). The discrepancies are likely due to the fact that Loh made vibrational assignments based on the molecular symmetry of MO_6 octahedral and TO_4 tetrahedral groups in the crystal structure and observations of Raman modes from similar atom clusters in other materials, whereas the eigenmodes calculated here are based on the complete crystal structure of phlogopite. Loh's general arguments agree to some extent with our findings, but discrepancies are seen in the details. According to Loh, Raman modes at frequencies greater than 300 cm^{-1} are dominated by T-O stretch motions within the tetrahedra. This argument is generally true from our findings,

but many Raman active eigenmodes in this frequency range have dominant M2 displacements mixed with tetrahedral sheet motions. According to Loh, MO_6 octahedral modes dominate at frequencies less than 200 cm^{-1}. We find that eigenmodes in this frequency range can contain octahedral motions mixed with lattice-like (F,OH) and tetrahedral sheet displacements. Loh assigns the 450 cm^{-1} IR mode to a tetrahedral stretch, where in each tetrahedron, the three Obr move in the opposite direction with respect to the single Onb. The closest IR modes from our calculation are the 474 cm^{-1} A_u and 408 cm^{-1} B_u modes (Tables 5 and 6, and Fig. 3b, right), which have atomic displacements that differ from Loh's description.

Far IR data for phlogopite in the 60 to 120 cm^{-1} range are presented by Tateyama et al. (1977). Modes found in the IR spectra at 90 and 156 cm^{-1} are reasonably close to B_u, modes calculated at 85 and 156 cm^{-1}. K-O stretch assignments were made to IR bands between 60 and 120 cm^{-1} due to the lack of similar bands in the spectra of K-free micas. These assignments are consistent with eigenmodes calculated for the 138 and 165 cm^{-1} A_u modes, as well as the 75 and 156 cm^{-1} B_u, modes (Tables 5 and 6). IR active eigenmodes within this frequency range may also be dominated by displacements from the M1 and M2 environments.

Internal sheet eigenmodes for phlogopite are generally quite different from eigenmodes calculated for the isolated six-membered rings in beryl or dioptase (Kim et al. 1995; McKeown et al. 1995), which have two non-bridging O atoms per tetrahedron. Only the most localized T-O stretch modes for the phlogopite structure can be considered similar to some displacements calculated for the silicate rings in cyclosilicates; in these few instances, v_n symbols, where n is 1 for T-O3 or 10 for T-O2, are used here to describe the motion (McKeown et al. 1993). Four eigenmodes having tetrahedral rotation, where the axis of rotation is parallel to the z axis, are similar to the bridging oxygen breathing modes determined for several of the cyclosilicate structures. In the case of phlogopite, three of the six bridging O atoms, in alternating fashion around the ring, move toward the ring center, while the other three move away (Fig. 3a left). Because the remaining eigenmodes are unique to the phlogopite structure, the motions are described as displacements of specific atom types (Tables 3 through 6).

Frequency vs. inter-sheet coupling relationships

All force constants not involving the T sites were reduced to zero to vibrationally decouple the sheets and to examine the vibrational behavior of isolated tetrahedral sheets in phlogopite. This was done by introducing a scale factor a, where $0 < \alpha < 1$. All force constants involving K, Ml, and M2 (i.e., k_i where i = 3, 4, 5, 6, 7, and 10 in Table 2) were multiplied by α; and a was then gradually reduced to zero, a technique introduced in our study of beryl (Kim et al. 1995).

The frequency vs. α relationships show different behavior for the different sets of eigenmodes in the frequency ranges described above. These relationships (not plotted here) indicate significant vibrational couplings of the sheets to the surrounding K and octahedral sites which parallel the characteristics of the eigenmodes described above and in Tables 3 through 6. The seven, six, five, and ten lowest frequency modes for the A_g, B_g, A_u, and B_u species, respectively, approach zero frequency as α approaches zero (isolated sheet). These lowest frequency modes are therefore lattice modes, which are dominated by motions within the K or octahedral environments, or by motions within the sheets that are driven by K or octahedral site displacements. All modes in the 350 to 850 cm^{-1} frequency range have slope changes in their respective frequency vs. α curves and exchange character when α varies from unity to zero; these modes are predominantly mixtures of internal sheet motions with K or octahedral site displacements. This behavior reflects the considerable coupling of internal sheet modes with those from the surrounding environment. Modes at frequencies greater than 1000 cm^{-1} show simple behavior as α is varied. No character exchange takes place for these most localized internal sheet modes.

ACKNOWLEDGMENTS

We thank J.E. Post and P. Pohwat of the Mineral Sciences Department, National Museum of Natural History, Smithsonian Institution for the phlogopite sample. We also thank R.J. Hemley and A. Goncharov of the Geophysical Laboratory, Carnegie Institution, for access to their micro-Raman facility and help with the collection of preliminary data. This work was supported in part by the U.S. Army Waterways Experiment Station and the Office of Naval Research. Certain commercial equipment, instruments, or materials are identified to specify experimental procedures. Such identification does not imply recommendation by the National Institute of Standards and Technology, nor does it imply that the materials or equipment are necessarily the best available for the purpose.

REFERENCES CITED

Clemens, J.D., Circone, S., Navrotsky, A., and McMillan, P.F. (1987) Phlogopite: high temperature solution calorimetry, thermodynamic properties, Al-Si and stacking disorder, and phase equilibria. Geochimica Cosmochimica Acta, 51, 2569–2578.

Fateley, W.G., Dollish, F.R., McDevitt, N,T., and Bentley, F.F. (1972) Infrared and Raman Selection Rules for Molecular and Lattice Vibrations: the Correlation Method, Wiley, New York.

Hazen, R.M. and Burnham, C.W. (1973) The crystal structures of one-layer phlogopite and annite. American Minerologist, 58, 889–900.

Kim, C.C., Bell, M.I., and McKeown, D.A. (1993) Vibrational analysis of benitoite and the Si_3O_9 ring. Physical Review B, 47, 7869–7877.

——— (1995) Vibrational analysis of beryl and the Si_6O_{18} ring. Physica B, 205, 193–208.

Loh, E. (1973) Optical vibrations in sheet silicates. Journal of Physics C: Solid State Physics 6, 1091–1104.

Loudon, R. (1964) Raman scattering from crystals. Advances in Physics, 13, 423–482.

McKeown, D.A. and Bell, M.I. (1997) Vibrational analysis of $BaCuSi_2O_6$ and implications for glass structure. Physical Review B, 56, 3114–3121.

——— (1998) Linked four-membered silicate rings: vibrational analysis of gillespite $BaFeSi_4O_{10}$ and implications for glass structure. Physics and Chemistry of Minerals, 25, 273–281.

McKeown, D.A., Bell, M.I., and Kim, C.C. (1993) Raman spectroscopy of silicate rings: benitoite and the three-membered ring. Physical Review B, 48, 16357–16365.

——— (1995) Vibrational analysis of dioptase and its puckered six-membered ring. Physics and Chemistry of Minerals, 22, 137–144.

McKeown, D.A., Nobles, A.C., and Bell, M.I. (1996) Vibrational analysis of wadeite $K_2ZrSi_3O_9$ and comparisons with benitoite $BaTiSi_3O_9$. Physical Review B, 54, 291–304.

Tateyama, H., Shimoda, S., and Sudo, T. (1977) Estimation of K-O distance and tetrahedral rotation angle of K-micas from far-infrared absorption spectral data. American Minerologist, 62, 534–539.

MANUSCRIPT RECEIVED JULY 13, 1998
MANUSCRIPT ACCEPTED DECEMBER 21, 1998
PAPER HANDLED BY HANS KEPPLER